Front. Phys. 13(3), 135101 (2018)
https://doi.org/10.1007/s11467-018-0749-3

RESEARCH ARTICLE

Discrete ellipsoidal statistical BGK model and Burnett equations

Yu-Dong Zhang[1,2], Ai-Guo Xu[2,3,†], Guang-Cai Zhang[2], Zhi-Hua Chen[1], Pei Wang[2]

[1] *Key Laboratory of Transient Physics, Nanjing University of Science and Technology, Nanjing 210094, China*
[2] *Laboratory of Computational Physics, Institute of Applied Physics and Computational Mathematics, Beijing 100088, China*
[3] *Center for Applied Physics and Technology, MOE Key Center for High Energy Density Physics Simulations, College of Engineering, Peking University, Beijing 100871, China*
Corresponding author. E-mail: [†] *Xu_Aiguo@iapcm.ac.cn*
Received November 8, 2017; accepted December 18, 2017

A new discrete Boltzmann model, the discrete ellipsoidal statistical Bhatnagar–Gross–Krook (ES-BGK) model, is proposed to simulate nonequilibrium compressible flows. Compared with the original discrete BGK model, the discrete ES-BGK has a flexible Prandtl number. For the discrete ES-BGK model in the Burnett level, two kinds of discrete velocity model are introduced and the relations between nonequilibrium quantities and the viscous stress and heat flux in the Burnett level are established. The model is verified via four benchmark tests. In addition, a new idea is introduced to recover the actual distribution function through the macroscopic quantities and their space derivatives. The recovery scheme works not only for discrete Boltzmann simulation but also for hydrodynamic ones, for example, those based on the Navier–Stokes or the Burnett equations.

Keywords discrete Boltzmann model, ellipsoidal statistical BGK, Burnett equations, nonequilibrium quantities, actual distribution function

PACS numbers 51.10.+y, 47.11.-j

Frontiers of Physics

1 Introduction

Rarefied gas flows are traditionally associated with spacecraft re-entry into planetary atmosphere, where the air is so thin that the applicability of the Navier–Stokes (NS) model is challenged [1–3]. Recently, the rarefied effect of flows in microchannels has attracted significant research interest due to the rapid development of microfluidic technologies such as microelectromechanical systems (MEMSs) [4, 5]. Generally, the rarefaction of flows can be measured by a dimensionless parameter, the Knudsen number (Kn), which is defined as the ratio of the mean free path of molecules to the characteristic length on which we focus. In summary, there are two types of rarefied-gas flows: one is the thin gas, which has a large molecular distance, such as the air in the high-altitude atmosphere [1], and the other is the flows with small characteristic length, such as shock wave and MEMS. In fact, according to the value of Kn, the flow can be divided into four categories: continuum flow (Kn $<$ 0.001), slip flow (0.001 $<$ Kn $<$ 0.1), transitional flow (0.1 $<$ Kn $<$ 10), and free molecular flow (Kn $>$ 10) [1, 4, 5].

As we know, NS equations are applicable to continuum and slip flow (with slip boundary conditions), but they fail to provide the correct viscous stress and heat flux in the transitional regime. The reason for the inapplicability of the NS equations in transitional flow is that the constitutive equations, i.e., Newton's viscosity law and the Fourier heat conduction law, are assumed to be linear, which is inapposite when the nonequilibrium (or rarefaction) effect is significant. The Burnett equations [3, 6], which are obtained from the Boltzmann equation through Chapman–Enskog (CE) expansion, have modified constitutive equations and can work in part of the transition flow zones. However, the Burnett equations often encounter numerical instabilities because of the high-order derivatives in the viscosity and heat flux terms [6].

It has been known that the Boltzmann equation is applicable for all of the four flow regimes mentioned above. Unfortunately, the original Boltzmann equation is too

*arXiv: 1711.02806.

complicated to be solved directly [7]. The multidimensional nature of the distribution function and collision operator poses a great challenge for the equation's numerical solution. Realistic numerical computations of the Boltzmann equation are based on probabilistic methods, such as the direct simulation Monte Carlo (DSMC) method [8], or deterministic fast numerical methods, such as the fast spectral method (FSM) [7]. In general, however, the computation cost is still too expensive for the direct solution of the Boltzmann equation. Therefore, a variety of simplified methods have been developed to approximate the solution of the Boltzmann equation, such as the unified gas-kinetic scheme (UGKS) [9, 10], the discrete velocity method (DVM) [11], the discrete unified gas-kinetic scheme (DUGKS) [12, 13], the lattice Boltzmann method (LBM) [14–18], and the discrete Boltzmann method (DBM) [19–21].

Recently, DBM has been developed as a nonequilibrium flow simulation tool and has been widely used in various flow conditions, including high-speed compressible flow, multiphase flow [22], flow instability [23, 24], and combustion and detonation [25, 26]. Besides the values and evolutions of conserved kinetic moments, the DBM presents also those of the most relevant nonconserved kinetic moments. The latter are helpful for understanding the constitutive relations for the former. Some of the new observations brought by DBM — for example, the nonequilibrium fine structures of shock waves [27] — have been confirmed and supplemented by the results of molecular dynamics [28–30]. It should be pointed out that the molecular dynamics simulations can also give a microscopic viewpoint of the origin of the slip near the boundary, such as the nonisotropic strong molecular evaporation flux from the liquid [31], which might help to develop more physically reasonable mesoscopic models for the slip-flow regime.

Generally, there are two steps to simplify the full Boltzmann equation. The first step is to simplify the collision operator. Several kinds of simplified collision operators, including the BGK model [32], ES-BGK model [33], Shakhov model [34], and Rykov model [35], are presented to substitute the collisional integral of the Boltzmann equation. Among those models, the BGK model is most extensively used because of its simplicity. However, the BGK model fails to give the proper Prandtl number (Pr), since the Pr in the BGK model is fixed to unity. The ES-BGK model, presented by Holway [33], employing a Gaussian distribution as the relaxation equilibrium state instead of the Maxwell distribution, is a modification of the BGK and possesses an adjustable Prandtl number. More importantly, the validity of the H-theorem for the ES-BGK model has been proved by Andries and his collaborators [36]. In addition, Zheng and Struchtrup [37] have found that the Burnett equations derived from the ES-BGK model completely agree with the Burnett equations from the full Boltzmann equation for Maxwell molecules. Thus, the ES-BGK model is preferable as far as the Pr effect is concerned.

The second step to simplify the Boltzmann equation is to develop a discrete model of the particle velocity space. According the modeling idea of the discrete Boltzmann method (DBM), the velocity space can be substituted by a limited number of particle velocities on the condition that the specific kinetic moments remain unchanged [19, 20]. The choice of those kinetic moments depends on the specific physical problem and technically the CE analysis. For example, only the 0^{th} to 4^{th} orders of velocity kinetic moments are needed for the DBM in the NS level. Inspired by the previous work about DBM [38], we present a framework of a discrete ES-BGK model, which contains the multiscale characteristic of DBM and can give a proper Prandtl number. As an example, the discrete ES-BGK model in the Burnett level is demonstrated and verified by numerical simulation.

The remainder of this paper is organized as follows. Section 2 demonstrates the derivation process of the ES-BGK model from the original Boltzmann equation. Section 3 shows the modeling of the discrete ES-BGK model, including the evolution equation, the required kinetic moments, and the discrete velocity model. Section 4 presents the relation between the new model and the Burnett equations, and the relations between nonequilibrium quantities and the constitutive equations in Burnett equations. Section 5 gives the simulation results of the new model for four test cases. Section 6 provides a new method to recover the actual velocity distribution function from the DBM approximately but quantitatively. Section 7 concludes the paper.

2 Ellipsoidal statistical BGK model

The original Boltzmann equation of single-component gases reads [2]

$$\frac{\partial f}{\partial t}+\boldsymbol{v}\cdot\frac{\partial f}{\partial \boldsymbol{r}}+\boldsymbol{a}\cdot\frac{\partial f}{\partial \boldsymbol{v}}=\left(\frac{\partial f}{\partial t}\right)_c, \tag{1}$$

where $\boldsymbol{a}$ is the external force per unit mass, and $(\frac{\partial f}{\partial t})_c$ is the collisional integral and can be represented as

$$\left(\frac{\partial f}{\partial t}\right)_c=\int_{-\infty}^{\infty}\int_0^{4\pi}(f'(\boldsymbol{v}_*)f'(\boldsymbol{v})-f(\boldsymbol{v}_*)f(\boldsymbol{v}))c_r\sigma \mathrm{d}\Omega \mathrm{d}\boldsymbol{v}_*, \tag{2}$$

where $f(\boldsymbol{v}_*)$ and $f(\boldsymbol{v})$ indicate the velocity distribution functions of two precollision molecules, and $f'(\boldsymbol{v}_*)$ and

$f'(\boldsymbol{v})$ are the corresponding velocity distribution functions of the two postcollision molecules, $c_r = |\boldsymbol{v}_* - \boldsymbol{v}|$ is the relative precollision velocity, and σ is the collision cross section.

To simplify the collisional integral, the $K(f)$ is introduced [33]

$$K(f) = \int_{-\infty}^{\infty}\int_{0}^{4\pi} f(\boldsymbol{v}_*)c_r\sigma \mathrm{d}\Omega \mathrm{d}\boldsymbol{v}_*. \tag{3}$$

Then, the collisional integral in Eq. (2) can be represented as

$$\left(\frac{\partial f}{\partial t}\right)_c = -K(f)[f(\boldsymbol{v}) - \boldsymbol{\psi}(f)], \tag{4}$$

where $\boldsymbol{\psi}(f)$ is functional of f and will be determined later. In fact, the physical meaning of the term $-K(f)f(\boldsymbol{v})\mathrm{d}\boldsymbol{v}\mathrm{d}\boldsymbol{r}$ is the number of "absorption" molecules by collisions from the range $\mathrm{d}\boldsymbol{v}\mathrm{d}\boldsymbol{r}$ around the point $(\boldsymbol{v}, \boldsymbol{r})$ in phase space per unit time, while $K(f)\boldsymbol{\psi}(f)\mathrm{d}\boldsymbol{v}\mathrm{d}\boldsymbol{r}$ is that of the "emission" molecules by collisions. The collision term needs to satisfy the conservation of mass, momentum, and energy, so it has

$$\int_{-\infty}^{\infty}\left(\frac{\partial f}{\partial t}\right)_c \theta(\boldsymbol{v})\mathrm{d}\boldsymbol{v} = 0, \tag{5}$$

where $\theta(\boldsymbol{v}) = 1, \boldsymbol{v}$, or $\boldsymbol{v}\cdot\boldsymbol{v}$. If we assume $K(f)$ to be independent of molecular velocity [33], the relations in Eq. (5) for three dimensions are equivalent to

$$\int_{-\infty}^{\infty}\boldsymbol{\psi}(\boldsymbol{v})\mathrm{d}\boldsymbol{v} = \rho, \tag{6}$$

$$\int_{-\infty}^{\infty}\boldsymbol{\psi}(\boldsymbol{v})\boldsymbol{v}\mathrm{d}\boldsymbol{v} = \rho\boldsymbol{u}, \tag{7}$$

$$\int_{-\infty}^{\infty}\boldsymbol{\psi}(\boldsymbol{v})(\boldsymbol{v}-\boldsymbol{u})\cdot(\boldsymbol{v}-\boldsymbol{u})\mathrm{d}\boldsymbol{v} = 3\rho RT. \tag{8}$$

To determine $\boldsymbol{\psi}(\boldsymbol{v})$ being subjected to the requirements of Eqs. (6)–(8), the entropy S is introduced, which can be used to measure the amount of uncertainty [33]. The S is defined as

$$S = -\int \boldsymbol{\psi}(\boldsymbol{v})\ln\boldsymbol{\psi}(\boldsymbol{v})\mathrm{d}\boldsymbol{v}. \tag{9}$$

If no further information about $\boldsymbol{\psi}(\boldsymbol{v})$ is known beyond the conditions of Eqs. (6)–(8), the most possible assignment of the $\boldsymbol{\psi}(\boldsymbol{v})$ is the one that maximizes the uncertainty S subject to these conditions. Using the Lagrangian multiplier method, one can obtain the form of $\boldsymbol{\psi}(\boldsymbol{v})$ as the Maxwellian distribution,

$$\boldsymbol{\psi}(\boldsymbol{v}) = \rho\frac{1}{(2\pi RT)^{3/2}}\exp\left[-\frac{|\boldsymbol{v}-\boldsymbol{u}|^2}{2RT}\right], \tag{10}$$

when S gets its maximum. To go a further step, let us consider that more restrictions are added to $\boldsymbol{\psi}(\boldsymbol{v})$, namely,

$$\int_{-\infty}^{\infty}\boldsymbol{\psi}(\boldsymbol{v})(v_\alpha - u_\alpha)(v_\beta - u_\beta)\mathrm{d}\boldsymbol{v} = \lambda_{\alpha\beta}, \tag{11}$$

where $\lambda_{\alpha\beta}$ is assumed to be known, and the specific form of $\lambda_{\alpha\beta}$ will be given later.

Under the conditions of Eq. (6), Eq. (7), and Eq. (11), when S gets its maximum, one can obtain the form of $\boldsymbol{\psi}(\boldsymbol{v})$ as

$$\boldsymbol{\psi}(\boldsymbol{v}) = \rho\frac{1}{(2\pi)^{3/2}|\lambda_{\alpha\beta}|^{1/2}}\exp\left[-\frac{1}{2}\lambda^{-1}_{\alpha\beta}(v_\alpha - u_\alpha)(v_\beta - u_\beta)\right], \tag{12}$$

which is the so-called ellipsoidal statistical model because $\boldsymbol{\psi}(\boldsymbol{v})$ in Eq. (12) is an ellipsoidal distribution in velocity space.

Now, the specific form of $\lambda_{\alpha\beta}$ is to be determined. First, the conservation of energy requires Eq. (8) to be satisfied so that the trace of $\lambda_{\alpha\beta}$ is

$$\lambda_{\alpha\alpha} = 3RT = \frac{1}{\rho}M^*_{\alpha\alpha}. \tag{13}$$

For convenience, $\lambda_{\alpha\beta}$ is chosen as a linear function of the second-order moments of f,

$$\lambda_{\alpha\beta} = \frac{1}{\rho}G_{\alpha\beta\gamma\lambda}M^*_{\gamma\lambda}, \tag{14}$$

where $M^*_{\alpha\beta} = \int_{-\infty}^{\infty} f(\boldsymbol{v})(v_\alpha - u_\alpha)(v_\beta - u_\beta)\mathrm{d}\boldsymbol{v}$ is the second-order central moment. Since the collision integral is an isotropic operator, $G_{\alpha\beta\gamma\lambda}$ must be an isotropic tensor. The most general form for the isotropic tensor of four orders can be represented as

$$G_{\alpha\beta\gamma\lambda} = a_1\delta_{\alpha\beta}\delta_{\gamma\lambda} + a_2\delta_{\alpha\gamma}\delta_{\beta\lambda} + a_3\delta_{\alpha\lambda}\delta_{\beta\gamma}. \tag{15}$$

Since $M^*_{\alpha\beta}$ is symmetric, Eq. (14) becomes

$$\lambda_{\alpha\beta} = \frac{1}{\rho}(a_1 M^*_{\gamma\gamma}\delta_{\alpha\beta} + bM^*_{\alpha\beta}), \tag{16}$$

where $b = a_2 + a_3$. From the relation of Eq. (13), it has $a_1 = \frac{1-b}{3}$. Thus, one can obtain

$$\lambda_{\alpha\beta} = (1-b)RT\delta_{\alpha\beta} + \frac{b}{\rho}M^*_{\alpha\beta} = RT\delta_{\alpha\beta} + \frac{b}{\rho}\tilde{M}^*_{\alpha\beta}, \tag{17}$$

where $\tilde{M}^*_{\alpha\beta} = M^*_{\alpha\beta} - \frac{1}{3}M_{\gamma\gamma}\delta_{\alpha\beta}$ is the traceless symmetric tensor of $M^*_{\alpha\beta}$.

From Eqs. (1), (4), (12), and (17), the ellipsoidal statistical model is obtained. However, there are still two parameters to be determined: K in Eq. (4) and b in

Eq. (17). From the CE multiscale expansion [33, 39] and the comparison with the NS equations, one can obtain

$$b = \frac{\mathrm{Pr} - 1}{\mathrm{Pr}}, \tag{18}$$

and

$$K = \mathrm{Pr}\,\frac{\rho RT}{\mu}. \tag{19}$$

where Pr is the Prandtl number and μ is the viscosity coefficient. In the latter part of this article, for convenience, the K is taken as $1/\tau$ where τ is the reciprocal of the molecular collision frequency.

3 Discrete ellipsoidal statistical BGK model

From the previous derivation, we know that the evolution equation of the ES-BGK model reads

$$\frac{\partial f}{\partial t} + v_\alpha \frac{\partial f}{\partial r_\alpha} = -\frac{1}{\tau}(f - f^{ES}), \tag{20}$$

when external forces are omitted, where f^{ES} is an ellipsoidal distribution as given in Eq. (12) with $\lambda_{\alpha\beta} = RT\delta_{\alpha\beta} + \frac{b}{\rho}\tilde{M}^*_{\alpha\beta}$. When $b = 0$ (i.e., Pr = 1), f^{ES} recovers to Maxwellian distribution f^{eq} which has a form as shown Eq. (10). In that case, the ellipsoidal statistical model recovers to the BGK model.

Combining the nonorganized momentum flux defined in [26], one can find that $\tilde{M}^*_{\alpha\beta}$ is essentially equivalent to $\Delta^*_{2,\alpha\beta}$ which corresponds to the viscous stress tensor in the macroscopic constitutive equations. The expression of $\lambda_{\alpha\beta}$ can therefore be rewritten as

$$\lambda_{\alpha\beta} = RT\delta_{\alpha\beta} + \frac{b}{\rho}\Delta^*_{2,\alpha\beta}. \tag{21}$$

The velocity space is substituted by a limited number of particle velocities, and the distribution function f is replaced by f_i where the subscript indicates the index of the discrete velocities. Then, the evolution equation of the discrete ES-BGK model is obtained

$$\frac{\partial f_i}{\partial t} + v_\alpha \frac{\partial f_i}{\partial r_{i\alpha}} = -\frac{1}{\tau}(f_i - f_i^{ES}). \tag{22}$$

From the CE expansion, hydrodynamic equations, including Euler, NS, and BGK–Burnett equations, can be obtained from Eq. (20). Specifically, the CE expansion indicates that, to obtain the NS and BGK–Burnett equations, the 0^{th} to 4^{th} orders and the 0^{th} to 5^{th} orders of the velocity kinetic moments of f^{eq} and f^{ES} are needed, respectively. In other words, only if those several orders of the velocity kinetic moments of f^{eq} and f^{ES} in integral form can be equally calculated from the corresponding summation form of f_i^{eq} and f_i^{ES} about particle velocities, can the NS (BGK–Burnett) equations be derived from Eq. (22). The 0^{th} to 5^{th} orders of the velocity kinetic moments of f_i^{ES}, $M_m^{ES}(m = 0, \cdots, 5)$, for the BGK–Burnett equations, are listed below:

$$M_0^{ES} = \sum_{i=1}^{N} f_i^{ES} = \rho, \tag{23}$$

$$M_{1,\alpha}^{ES} = \sum_{i=1}^{N} f_i^{ES} v_{i\alpha} = \rho u_\alpha, \tag{24}$$

$$M_{2,\alpha\beta}^{ES} = \sum_{i=1}^{N} f_i^{ES} v_{i\alpha} v_{i\beta} = \rho(J_{\alpha\beta} + u_\alpha u_\beta), \tag{25}$$

$$\begin{aligned} M_{3,\alpha\beta\gamma}^{ES} &= \sum_{i=1}^{N} f_i^{ES} v_{i\alpha} v_{i\beta} v_{i\gamma} \\ &= \rho(u_\alpha J_{\beta\gamma} + u_\beta J_{\alpha\gamma} + u_\gamma J_{\beta\alpha} + u_\alpha u_\beta u_\gamma), \end{aligned} \tag{26}$$

$$\begin{aligned} M_{4,\alpha\beta\gamma\chi}^{ES} &= \sum_{i=1}^{N} f_i^{ES} v_{i\alpha} v_{i\beta} v_{i\gamma} v_{i\chi} \\ &= \rho(J_{\alpha\beta\gamma\chi} + J_{\alpha\beta} u_\gamma u_\chi + J_{\alpha\gamma} u_\beta u_\chi \\ &\quad + J_{\alpha\chi} u_\beta u_\gamma + J_{\beta\gamma} u_\alpha u_\chi + J_{\beta\chi} u_\alpha u_\gamma \\ &\quad + J_{\gamma\chi} u_\alpha u_\beta + u_\alpha u_\beta u_\gamma u_\chi), \end{aligned} \tag{27}$$

$$M_{5.3,\alpha\beta\gamma}^{ES} = \sum_{i=1}^{N} f_i^{ES} v_{i\alpha} v_{i\beta} v_{i\gamma} \frac{v_{i\chi}^2}{2} = \frac{1}{2} M_{5,\alpha\beta\gamma\chi\chi}^{ES}, \tag{28}$$

where $J_{\alpha\beta} = \lambda_{\alpha\beta}$, $J_{\alpha\beta\gamma\xi} = \lambda_{\alpha\beta}\lambda_{\gamma\xi} + \lambda_{\alpha\gamma}\lambda_{\beta\xi} + \lambda_{\alpha\xi}\lambda_{\beta\gamma}$, and $\lambda_{\alpha\beta}$ can be found in Eq. (21). Besides, the third-order tensor $M_{5,\alpha\beta\gamma\chi\chi}^{ES}$ is contracted from $M_{5,\alpha\beta\gamma\lambda\xi}^{ES}$ which reads

$$\begin{aligned} M_{5,\alpha\beta\gamma\lambda\xi}^{ES} = \rho(&J_{\alpha\beta\gamma\lambda} u_\xi + J_{\alpha\beta\gamma\xi} u_\lambda + J_{\alpha\beta\lambda\xi} u_\gamma + J_{\alpha\gamma\lambda\xi} u_\beta \\ &+ J_{\beta\gamma\lambda\xi} u_\alpha + J_{\alpha\beta} u_\gamma u_\lambda u_\xi + J_{\alpha\gamma} u_\beta u_\lambda u_\xi \\ &+ J_{\alpha\lambda} u_\beta u_\gamma u_\xi + J_{\alpha\xi} u_\beta u_\gamma u_\lambda + J_{\beta\gamma} u_\alpha u_\lambda u_\xi \\ &+ J_{\beta\lambda} u_\alpha u_\gamma u_\xi + J_{\beta\xi} u_\alpha u_\gamma u_\lambda + J_{\gamma\lambda} u_\alpha u_\beta u_\xi \\ &+ J_{\gamma\xi} u_\alpha u_\beta u_\lambda + J_{\lambda\xi} u_\alpha u_\beta u_\gamma \\ &+ u_\alpha u_\beta u_\gamma u_\lambda u_\xi). \end{aligned}$$

The kinetic moments of f_i^{eq}, $M_m(m = 0, \cdots, 5)$, can also be obtained from Eqs. (23)–(28) when $b = 0$ in $\lambda_{\alpha\beta}$. Those kinetic moment equations can be written in a matrix form, i.e.,

$$\boldsymbol{C} \cdot \boldsymbol{f}^{ES} = \boldsymbol{M}^{ES}, \tag{29}$$

where $\boldsymbol{C}$ is the coefficient matrix whose elements are determined by discrete velocities, $\boldsymbol{f}^{ES}$ is a vector of discrete velocity distribution function whose number of components equals to the number of discrete velocities, and $\boldsymbol{M}^{ES}$ is a vector of the kinetic moments.

It can be seen that, once the discrete velocities are determined, the form of the coefficient matrix $\boldsymbol{C}$ is known.

The matrix $\boldsymbol{C}$ is a square matrix when the number of discrete velocities exactly equals the number of independent kinetic moments; otherwise, it is not a square matrix. Nevertheless, once the discrete velocities are known, the discrete ellipsoidal statistical distribution function f_i^{ES} can be solved from Eq. (29). The choice of the discrete velocity depends on the compromise among the following points: (i) numerical efficiency, (ii) numerical stability, and (iii) the extent to which the local symmetry should be kept. The third point relies on the specific physical problem under consideration.

In this study, as an example, two kinds of DVM for the two-dimensional (2D) case are presented. Considering that the number of independent kinetic moments is 19 in Eqs. (23)–(28) for the 2D case, the first DVM contains 19 discrete velocities and is denoted by D2V19. From the above discussion, we know that the coefficient matrix $\boldsymbol{C}$ is square for this kind of DVM. In this case, the square matrix $\boldsymbol{C}$ must be full rank to ensure that Eq. (29) has a solution. Therefore, the discrete velocities model is chosen as in Fig. 1(a) and the special value of each discrete velocity is given in Eq. (30). The other DVM contains 36 discrete velocities and is denoted by D2V36, which is shown in Fig. 1(b), and the special value of corresponding discrete velocity can be found in Eq. (31).

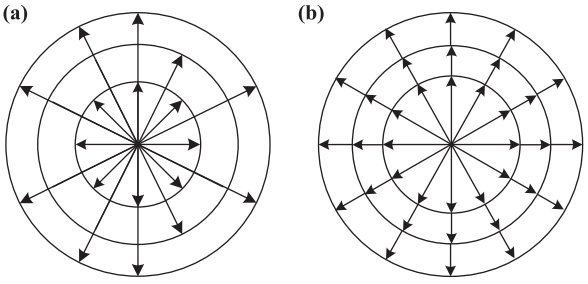

Fig. 1 Schematic of discrete velocity model. **(a)** D2V19 model; **(b)** D2V36 model.

$$\boldsymbol{v}=(v_{ix},v_{iy})=\begin{cases}(0,0), & i=1\\ c\left(\cos\dfrac{(i-2)\pi}{4},\sin\dfrac{(i-2)\pi}{4}\right), & i=2\text{–}9\\ a\left(\cos\dfrac{(i-9)\pi}{6},\sin\dfrac{(i-9)\pi}{6}\right)\begin{cases}a=2c, & i=10\text{–}14\ \&\ i\neq 11\\ a=\dfrac{3}{2}c, & i=11\end{cases}\\ a\left(\cos\dfrac{(i-8)\pi}{6},\sin\dfrac{(i-8)\pi}{6}\right)\begin{cases}a=2c, & i=15\text{–}19\ \&\ i\neq 18\\ a=\dfrac{3}{2}c, & i=18\end{cases}\end{cases} \tag{30}$$

$$\boldsymbol{v}=(v_{ix},v_{iy})=\begin{cases}c\left(\cos\dfrac{(i-1)\pi}{6},\sin\dfrac{(i-1)\pi}{6}\right), & i=1\text{–}12\\ 2c\left(\cos\dfrac{(i-13)\pi}{6},\sin\dfrac{(i-13)\pi}{6}\right), & i=13\text{–}24\\ 3c\left(\cos\dfrac{(i-25)\pi}{6},\sin\dfrac{(i-25)\pi}{6}\right), & i=25\text{–}36\end{cases} \tag{31}$$

where c is an adjustable parameter.

4 Ellipsoidal statistical BGK model and Burnett equations

Because the velocity distribution function can be expanded around its local thermodynamic equilibrium state

$$f_i=f_i^{eq}+\varepsilon f_i^{(1)}+\varepsilon^2 f_i^{(2)}+\cdots, \tag{32}$$

and the f^{ES} can also be expanded around the local equilibrium distribution function

$$f_i^{ES}=f_i^{eq}+\varepsilon f_i^{ES(1)}+\varepsilon^2 f_i^{ES(2)}+\cdots, \tag{33}$$

the general equations of hydrodynamics can be obtained from Eq. (22), which reads [26]

$$\frac{\partial\rho}{\partial t}+\frac{\partial(\rho u_\alpha)}{\partial r_\alpha}=0, \tag{34}$$

$$\frac{\partial(\rho u_\alpha)}{\partial t}+\frac{\partial(\rho u_\alpha u_\beta+p\delta_{\alpha\beta})}{\partial r_\beta}+\frac{\partial}{\partial r_\beta}\Delta^*_{2,\alpha\beta}=0, \tag{35}$$

$$\frac{\partial(\rho E)}{\partial t}+\frac{\partial[(\rho E+p)u_\alpha]}{\partial r_\alpha}+\frac{\partial}{\partial r_\alpha}(u_\beta\Delta^*_{2,\alpha\beta}+\Delta^*_{3.1,\alpha})=0, \tag{36}$$

where the nonequilibrium quantities $\Delta^*_{2,\alpha\beta}$ and $\Delta^*_{3.1,\alpha}$ are the so-called nonorganized momentum flux (NOMF) and nonorganized energy flux (NOEF).

In the NS level, $\Delta^*_{2,\alpha\beta}$ and $\Delta^*_{3.1,\alpha}$ are approximately

equal to $\Delta^{*(1)}_{2,\alpha\beta}$ and $\Delta^{*(1)}_{3.1,\alpha}$, respectively. That is

$$\Delta^{*}_{2,\alpha\beta} \approx \Delta^{*(1)}_{2,\alpha\beta} = \sum_{i=1}^{N} \varepsilon f_i^{(1)} (v_{i\alpha} - u_\alpha)(v_{i\beta} - u_\beta), \tag{37}$$

$$\Delta^{*}_{3.1,\alpha} \approx \Delta^{*(1)}_{3.1,\alpha} = \frac{1}{2} \sum_{i=1}^{N} \varepsilon f_i^{(1)} (v_{i\gamma} - u_\gamma)^2 (v_{i\alpha} - u_\alpha), \tag{38}$$

where N is the number of discrete velocities.

From the CE expansion, the $f_i^{(1)}$ can be repressed by f_i^{eq},

$$\varepsilon f_i^{(1)} = -\tau \left(\varepsilon \frac{\partial f_i^{eq}}{\partial t_1} + v_\alpha \varepsilon \frac{\partial f_i^{eq}}{\partial r_{1\alpha}} \right) + \varepsilon f_i^{ES(1)}, \tag{39}$$

where time multiscale expansion has been adopted, i.e., $\frac{\partial}{\partial t} = \varepsilon \frac{\partial}{\partial t_1} + \varepsilon^2 \frac{\partial}{\partial t_2} + \cdots$, $\frac{\partial}{\partial r_\alpha} = \varepsilon \frac{\partial}{\partial r_{1\alpha}}$, and t_1 and t_2 are two independent time scales. Then we can obtain

$$\Delta^{*}_{2,\alpha\beta} \approx \Delta^{*(1)}_{2,\alpha\beta} = 2\mu \frac{\partial u_{<\alpha}}{\partial r_{\beta>}}, \tag{40}$$

$$\Delta^{*}_{3.1,\alpha} \approx \Delta^{*(1)}_{3.1,\alpha} = \kappa \frac{\partial T}{\partial r_\alpha}, \tag{41}$$

where $\mu = \frac{1}{1-b}\tau p$, $\kappa = c_p \tau p$, c_p is the specific heat ratio at constant pressure, and $\frac{\partial u_{<\alpha}}{\partial r_{\beta>}}$ is the trace-free tensors, which reads $\frac{\partial u_{<\alpha}}{\partial r_{\beta>}} = \frac{1}{2}(\frac{\partial u_\alpha}{\partial r_\beta} + \frac{\partial u_\beta}{\partial r_\alpha}) - \frac{1}{D}\frac{\partial u_\gamma}{\partial r_\gamma}\delta_{\alpha\beta}$, where D is the spatial dimension [39].

In the Burnett level, the $\Delta^{*}_{2,\alpha\beta}$ and $\Delta^{*}_{3.1,\alpha}$ are approximately equal to $\Delta^{*(1)}_{2,\alpha\beta} + \Delta^{*(2)}_{2,\alpha\beta}$ and $\Delta^{*(1)}_{3.1,\alpha} + \Delta^{*(2)}_{3.1,\alpha}$, respectively,

$$\Delta^{*}_{2,\alpha\beta} \approx \Delta^{*(1)}_{2,\alpha\beta} + \Delta^{*(2)}_{2,\alpha\beta}, \tag{42}$$

$$\Delta^{*}_{3.1,\alpha} \approx \Delta^{*(1)}_{3.1,\alpha} + \Delta^{*(2)}_{3.1,\alpha}, \tag{43}$$

where $\Delta^{*(2)}_{2,\alpha\beta}$ and $\Delta^{*(2)}_{3.1,\alpha}$ read

$$\Delta^{*(2)}_{2,\alpha\beta} = \sum_{i=1}^{N} \varepsilon^2 f_i^{(2)} (v_{i\alpha} - u_\alpha)(v_{i\beta} - u_\beta), \tag{44}$$

$$\Delta^{*(2)}_{3.1,\alpha} = \frac{1}{2} \sum_{i=1}^{N} \varepsilon^2 f_i^{(2)} (v_{i\gamma} - u_\gamma)^2 (v_{i\alpha} - u_\alpha). \tag{45}$$

Similarly, $f_i^{(2)}$ can be repressed by $f_i^{(1)}$,

$$\varepsilon^2 f_i^{(2)} = -\tau \left(\varepsilon^2 \frac{\partial f_i^{eq}}{\partial t_2} + \varepsilon \frac{\partial f_i^{(1)}}{\partial t_1} + v_\alpha \varepsilon \frac{\partial f_i^{(1)}}{\partial r_\alpha} \right) + \varepsilon^2 f_i^{ES(2)}, \tag{46}$$

where $f_i^{(1)}$ can be further substituted by f_i^{eq} using Eq. (39).

If the viscosity μ is adopted as a function of temperature [37], the relaxation time τ has a relation with macroscopic quantities, which reads

$$\tau = (1-b)\frac{\mu}{p} = \tau_0 \rho^{-1} T^{\beta-1}, \tag{47}$$

where $\tau_0 = \frac{(1-b)\mu_0}{T_0^\beta}$ is the reference relaxation time, and the $\Delta^{*(2)}_{2,\alpha\beta}$ and $\Delta^{*(2)}_{3.1,\alpha}$ can be obtained as the same form as Eq. (28) in [37]. As a preliminary study, however, we will take the relaxation time τ as a constant in the following study. In this case, the expressions for $\Delta^{*(2)}_{2,\alpha\beta}$ and $\Delta^{*(2)}_{3.1,\alpha}$ in 2D read

$$\begin{aligned}\Delta^{*(2)}_{2,\alpha\beta} = \frac{2\tau^2}{(1-b)^2} \Bigg[& (1-b)\rho \frac{\partial T}{\partial r_{<\alpha}} \frac{\partial T}{\partial r_{\beta>}} - \rho T b \frac{\partial^2 T}{\partial r_{<\alpha} \partial r_{\beta>}} \\ & - \rho T \frac{\partial u_\gamma}{\partial r_{<\alpha}} \frac{\partial u_\gamma}{\partial r_{\beta>}} + \frac{T^2}{\rho} \frac{\partial \rho}{\partial r_{<\alpha}} \frac{\partial \rho}{\partial r_{\beta>}} \\ & - bT \frac{\partial T}{\partial r_{<\alpha}} \frac{\partial \rho}{\partial r_{\beta>}} - T^2 \frac{\partial^2 \rho}{\partial r_{<\alpha} \partial r_{\beta>}} \Bigg],\end{aligned} \tag{48}$$

$$\begin{aligned}\Delta^{*(2)}_{3.1,\alpha} = \frac{\tau^2}{1-b} p \Bigg[& (2+b)\frac{\partial T}{\partial r_\beta}\frac{\partial u_\beta}{\partial r_\alpha} + (6-3b)\frac{\partial u_\alpha}{\partial r_\beta}\frac{\partial T}{\partial r_\beta} \\ & - (6-3b)\frac{\partial u_\beta}{\partial r_\beta}\frac{\partial T}{\partial r_\alpha} - 2(1-b)T\frac{\partial^2 u_\beta}{\partial r_\alpha \partial r_\beta} \\ & + T\frac{\partial^2 u_\alpha}{\partial r_\beta \partial r_\beta} \Bigg],\end{aligned} \tag{49}$$

where the angle brackets in the subscript denote the trace-free tensor, as an example $\frac{\partial^2 T}{\partial r_{<\alpha}\partial r_{\beta>}} = \frac{\partial^2 T}{\partial r_\alpha \partial r_\beta} - \frac{1}{2}\left(\frac{\partial^2 T}{\partial x^2} + \frac{\partial^2 T}{\partial y^2}\right)\delta_{\alpha\beta}$ for 2D. For more details about the trace-free tensor, refer to Appendix A 2.2 in Ref. [39].

5 Numerical results

In this section, we validate the proposed discrete ES-BGK model by several tests, including viscous sod shock tube, no-slip thermal Couette flow, a Mach 3 wind tunnel with a step, and the steady shock wave. For the first two cases, the D2V19 model is adopted. The results can be used to verify the ability of the new model to describe different Prandtl number situations. For the latter two tests, the D2V36 model is adopted. The simulation of the Mach 3 wind tunnel with a step can be used to verify the applicability of the new model to the 2D shock wave cases and the calculation of steady shock wave shows the relations between viscous stress (heat flux) in the Burnett level and the NOMF (NOEF).

5.1 Viscous sod shock tube

The initial conditions of the sod tube are adopted, which read

$$\begin{cases} (\rho, u_x, u_y, T)_L = (1, 0, 0, 1), \\ (\rho, u_x, u_y, T)_R = (0.125, 0, 0, 0.8). \end{cases} \tag{50}$$

The simulation area is divided into two parts, and the subscripts "L" and "R" in Eq. (50) are the initial con-

ditions of the left half part and right half part, respectively. The D2V19 model in Fig. 1(a) is adopted and $c = 2.0$. Simulations are carried out under the condition: the space step $\Delta x = \Delta y = 1 \times 10^{-3}$, the number of mesh $Nx \times Ny = 1000 \times 1$, the time step $\Delta t = 2 \times 10^{-6}$, and the relaxation time $\tau = 2 \times 10^{-4}$. The free inflow and free outflow boundary conditions are adopted in left and right, respectively. For all simulations reported in this paper, the second-order NND scheme is adopted to solve the space derivation, and the first-order forward difference is used to solve the time derivation in Eq. (22).

Five cases with different kinds of Prandtl numbers are calculated. Figure 2 shows the results of velocity and temperature profiles at $t = 0.18$. The Riemann solutions (the solid line) are also plotted for comparison. The Riemann solutions are calculated based on the Euler equations, which do not include the effects of viscosity and heat flux, while the simulation results (the symbols) contain those. Thus, there exist distinct transition zones around the discontinuities for the velocity and temperature profiles of simulation results.

Figure 3 shows the profiles of viscous stress and heat flux. The NOMF and the NOEF are also plotted for comparison. The viscous stress and heat flux are calculated by Eqs. (40) and (41), respectively. The values of viscous stress show significant difference, whereas the values of heat flux are the same for different Prandtl numbers. It can be observed that the values of NOMF agree well with viscous stresses in the NS level, and the effect of the Prandtl number is naturally included in the NOMF.

5.2 No-slip thermal Couette flow

Couette flow with a temperature gradient is a good test to describe the viscous heat-conducting flow. Consider a gas flow between two parallel walls with the bottom fixed and the top wall moving with a speed U in the x direction. The temperature of the bottom and the top wall are fixed with T_0 and T_1, respectively. According to incompressible NS equations, the steady-state analytic dimensionless temperature distribution reads [40, 41]

$$\frac{T - T_0}{T_1 - T_0} = \frac{y}{H} + \frac{\Pr \mathrm{Ec}}{2} \frac{y}{H} \left(1 - \frac{y}{H}\right), \tag{51}$$

where Ec is the Ecker number, $\mathrm{Ec} = \frac{U^2}{C_p(T_1 - T_0)}$.

The D2V19 model in Fig. 1(a) is adopted, and $c = 1.6$. The simulation distance of two walls is $H = 1.0$ and the number of the mesh is $Nx \times Ny = 1 \times 500$. The bottom wall is fixed with a temperature $T_0 = 1.0$, while the moving velocity of the top wall is $U = 0.2$ with a temperature $T_1 = 1.001$ (i.e., $\mathrm{Ec} = 20$). The initial density of the gas inside the channel is 1.0, and the initial velocity is $u(y) = yU/H$, so the fluid in the channel can be approximated as incompressible. No-slip wall boundary conditions are adopted to the bottom and the top [42]. Different Prandtl numbers and Ecker numbers are simulated and compared with analytical solutions. The Ecker number is adjusted by T_1; for example, when $T_1 = 1.005$, $\mathrm{Ec} = 4$.

Figure 4 gives the simulation results. Figures 4(a) and (b) present the results in the cases with different Prandtl numbers and Ecker numbers, respectively. The simulation results fit the analytic solutions very well, from which we can conclude that the Prandtl number correction in discrete ES-BGK does work well.

5.3 A Mach 3 wind tunnel with a step

This two-dimensional test was first introduced by Emery and is widely used to verify the capacity of the new model to capture shock wave in the 2D case [43]. The problem begins with uniform Mach 3 flow in a wind tunnel containing a step. The tunnel has a length of 3 and a width of 1. The step is located at 0.6 from the entrance with

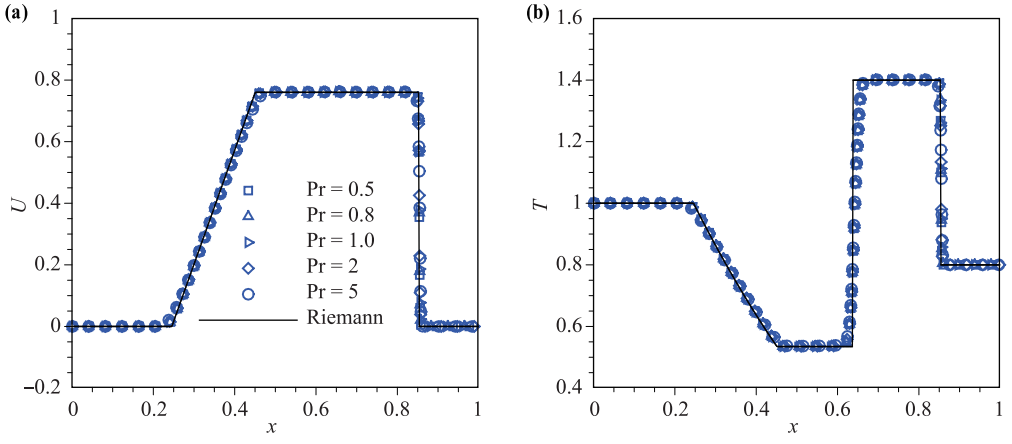

Fig. 2 Profiles of velocity and temperature of sod shock tube at $t = 0.18$: **(a)** velocity, **(b)** temperature. The simulation results are denoted by symbols, and the Riemann solution is represented by solid lines.

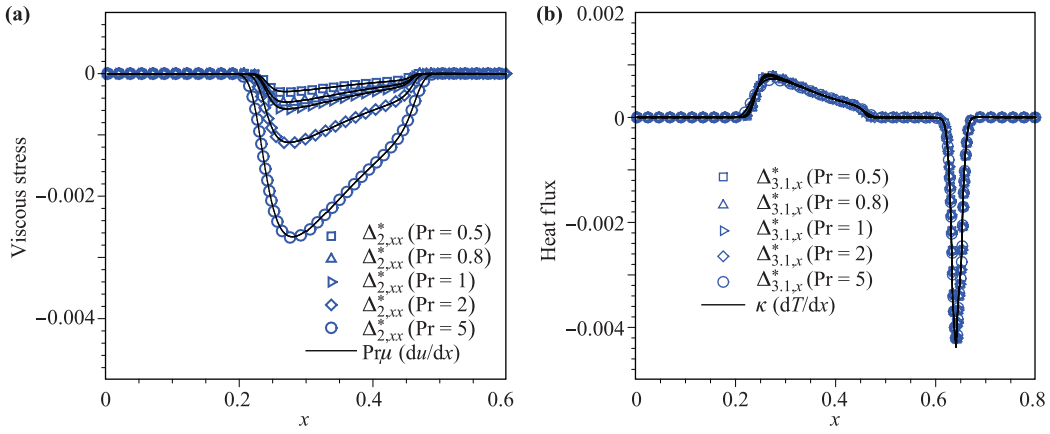

Fig. 3 Profiles of viscous stress and heat flux of sod shock tube: **(a)** viscous stress, **(b)** heat flux. The NOMF and NOEF are denoted by symbols and the viscous stress and flux are represented by solid lines.

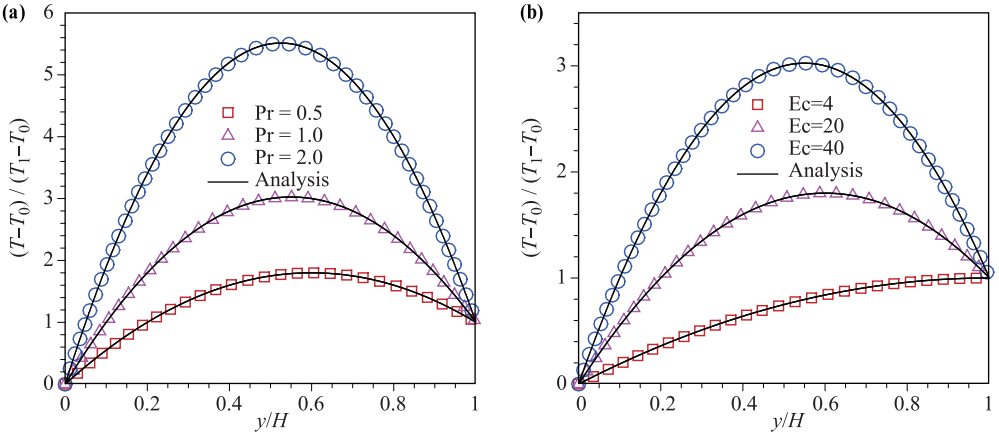

Fig. 4 The temperature spatial distribution on steady state for different Prandtl numbers and Ecker numbers: **(a)** different Prandtl numbers, **(b)** different Ecker numbers. The solid lines denote the analytic solutions, and the symbols are simulation results.

a width of 0.2. Initially, the wind tunnel is filled with a gas with density $\rho_0 = 2.0$, pressure $p_0 = 1.0$, and velocity $u_0 = 3.0$. The inflow and the outflow boundary conditions are adopted in the left and the right boundary. Along the walls of the tunnel, reflecting boundary conditions are applied. As demonstrated in Ref. [43], the corner of the step is the center of a rarefaction and, hence, is a singular point of the flow. Just as a qualitative study, we have not done anything special at the singular point.

The D2V36 model in Fig. 1(b) is used (with $c = 2.0$) to ensure the symmetry of the discrete velocity, which has a significant effect on the numerical stability of the simulation, especially for 2D problem. The results are shown in Fig. 5. The contours of density and pressure are presented in Figs. 5(a) and (b), respectively. The results calculated by numerically solving the NS equations are also plotted at the bottom half of the figures for comparison. It can be seen that the results of the new model are consistent with those from the NS equations. The simulation results show that the discrete ES-BGK with the D2V36 model can be used to simulate the two-dimensional high-speed compressible problems.

5.4 Nonequilibrium effects of the shock wave

In the above cases, the validation of the discrete ES-BGK model in the NS level is verified. In fact, as we have mentioned, the new model also works in the Burnett level. To verify the characteristic of the nonlinear constitutive relation of the new model, a one-dimensional steady shock wave is simulated, and the viscous stress and heat flux around the wave front are presented and discussed. The initial state is set by Hugoniot relation with 1.5 Mach,

$$\begin{cases} (\rho, u_x, u_y, T)_L = (1.5882, 0.7857, 0, 1.6790), \\ (\rho, u_x, u_y, T)_R = (1.0, 0, 0, 1.0). \end{cases} \tag{52}$$

At beginning, the shock is located at $x = 0.02$. The D2V36 model in Fig. 1(b) is adopted, and $c = 1.5$. The computation is carried out with the mesh number $Nx \times$

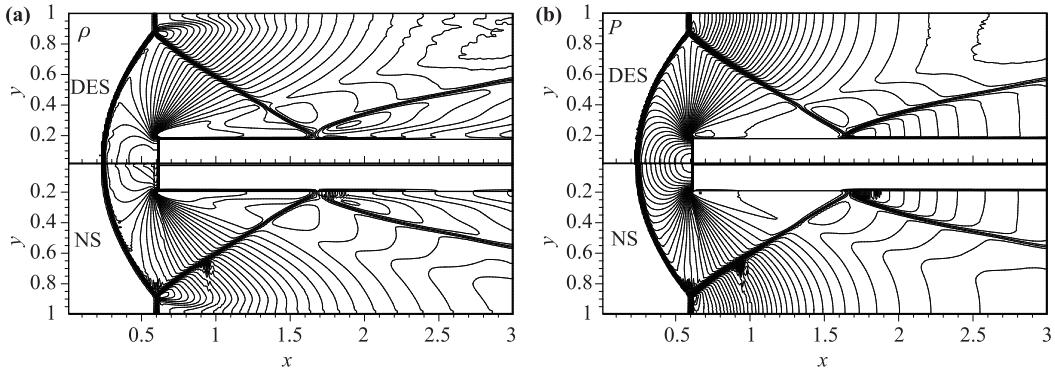

Fig. 5 The contours of the density and pressure of steady state for the Mach 3 step problem: **(a)** density contour, **(b)** pressure contour. The upper half of each figure is obtained by the discrete ES-BGK, and the bottom half is the result of NS.

$Ny = 5000 \times 1$. The space step is $\Delta x = \Delta y = 2 \times 10^{-4}$, the time step is $\Delta t = 1 \times 10^{-6}$, and the relaxation time is $\tau = 1 \times 10^{-3}$. The free inflow and outflow boundary condition are adopted in the left and right boundaries, respectively.

Three different Prandtl numbers are simulated, and the profiles of density and temperature in the steady state are presented in Fig. 6. Profiles for different Prandtl numbers nearly intersect at one point around $x = 0.38$ for both density and temperature. In front of the intersection ($x < 0.38$), the larger values of density and temperature correspond to the smaller Prandtl number, while, behind the intersection, the larger values of density and temperature correspond to the larger Prandtl number. The difference between the three Prandtl numbers is not significant in Fig. 6, so the corresponding values of viscous stress and heat flux around the shock front are given in Fig. 7.

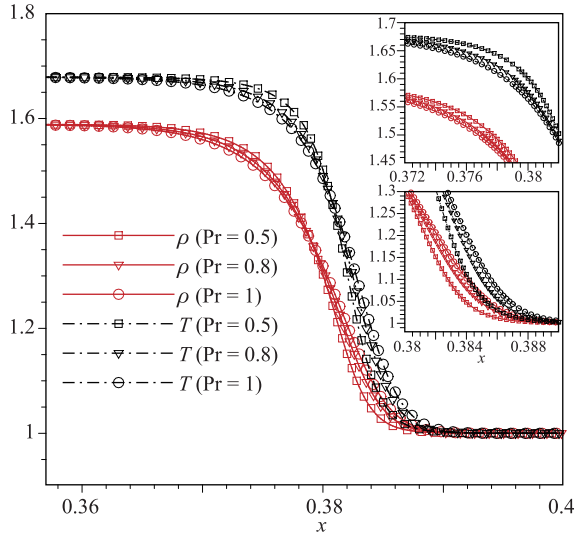

Fig. 6 Profiles of density and temperature in the steady state of a 1.5 Mach shock wave for different Prandtl numbers. The solid lines with symbols are density profiles, and the dash dot lines with symbols denote temperature profiles. Different Prandtl numbers are distinguished by different shapes of symbols.

The profiles of the NS viscous stress (heat flux), the Burnett viscous stress (heat flux), and the NOMF (NOEF) are plotted in the same figure for comparison. From Fig. 7, we can observe that the NOMF coincides well with the NS and the Burnett viscous stress when the system is near the equilibrium state. However, with the increase of the nonequilibrium effects, the NS viscous stress first deviates from NOMF, while the Burnett viscous stress still coincides well with the NOMF. With the further increase of the nonequilibrium effect, the Burnett viscous stress also deviates from the NOMF around the maximum point. The characteristics of heat flux and NOEF are similar.

From Fig. 7, we can conclude that the new model is in the Burnett level. Taking account of the second-order term, the viscous stress and heat flux are more approximate to the NOEF and NOMF than the first-order ones when the nonequilibrium strength is much higher within a certain extent.

6 Recovering of the velocity distribution function

In Ref. [27], the qualitative information on the actual distribution function was drawn using the components of the nonequilibrium quantities, $\mathbf{\Delta}_m^*$. Recently, it has been found that the actual distribution function, to some extent, can be recovered quantitatively, although the discrete distribution function is not a real one in the evolutionary equation of DBM. The recovering of the velocity distribution function is often needed, because the distribution function can be used to characterize the nonequilibrium state of the flow system.

According to the CE expansion, the actual velocity

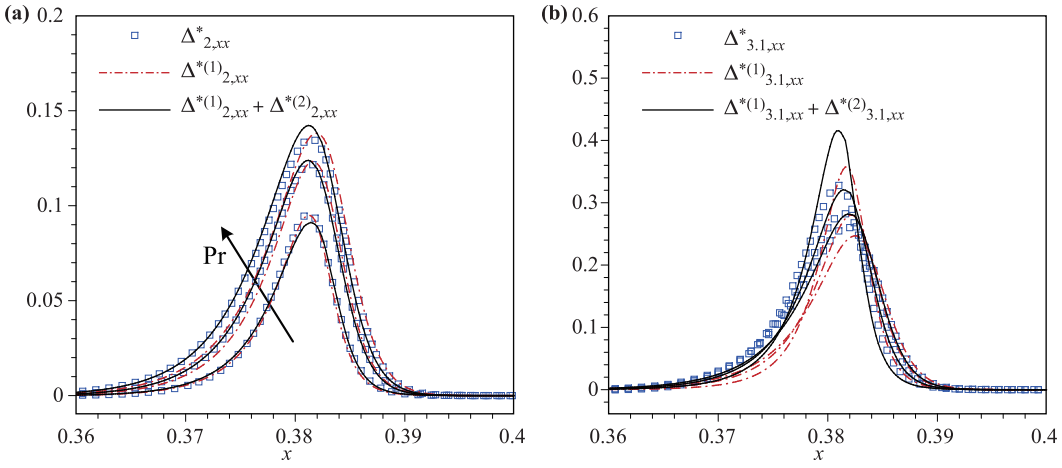

Fig. 7 Comparisons of viscous stress (heat flux) and NOMF (NOEF): **(a)** profiles of viscous stress and NOMF, **(b)** profiles of heat flux and NOEF. Dash dot lines are the NS viscous stress and heat flux, solid lines denote the Burnett viscous stress and heat flux, and the symbols represent the NOMF and NOEF. The arrow points to the increasing direction of the Pr.

distribution function can be expanded as a Taylor series near the equilibrium state, which reads (for the BGK model)

$$f = f^{eq} + \varepsilon f^{(1)} + \varepsilon^2 f^{(2)} + \cdots, \tag{53}$$

where ε is a small quantity that has a positive correlation with the dimensionless relaxation time (or Knudsen number). When $\varepsilon \to 0$ which means the system reaches its equilibrium in an infinitely small amount of time, it seems that the velocity distribution function is always in its equilibrium state. With the increase of ε, such as $\varepsilon = 0.01$, the term with first order of ε may not be ignored, but the term with second order of ε^2 is still so insignificant that it can be ignored and the truncated terms would not make much difference. The larger the value of ε, the more terms in Eq. (53) need to be kept, and the more deviation of the actual distribution function away from its equilibrium state. Our discussions below are limited to the situation near the equilibrium state.

First, in the NS level, from the CE expansion, we know that $f = f^{eq} + \varepsilon f^{(1)}$ and

$$\varepsilon f^{(1)} = -\tau \left(\varepsilon \frac{\partial f^{eq}}{\partial t_1} + v_\alpha \varepsilon \frac{\partial f^{eq}}{\partial r_{1\alpha}} \right). \tag{54}$$

Since the equilibrium distribution function f^{eq} can be expressed by ρ, u_α, and T, the derivative of f^{eq} can turn into the derivative of ρ, u_α, and T.

$$f^{(1)} = f^{eq}\left[D_\rho \left(\frac{\partial \rho}{\partial t_1} + v_\alpha \frac{\partial \rho}{\partial r_{1\alpha}} \right) + D_T \left(\frac{\partial T}{\partial t_1} + v_\alpha \frac{\partial T}{\partial r_{1\alpha}} \right) + D_{u_\beta} \left(\frac{\partial u_\beta}{\partial t_1} + v_\alpha \frac{\partial u_\beta}{\partial r_{1\alpha}} \right) \right] \tag{55}$$

with $D_\rho = \frac{1}{\rho}$, $D_T = \left[-\frac{D}{2}\frac{1}{T} + \frac{|v_\alpha - u_\alpha|^2}{2RT^2} \right]$, and $D_{u_\beta} = -\frac{(v_\beta - u_\beta)}{RT}$. In addition, the time partial derivatives in Eq. (55) can be represented by the space partial derivative through the Euler equations, which read

$$\frac{\partial \rho}{\partial t_1} = -\rho \frac{\partial u_\alpha}{\partial r_{1\alpha}} - u_\alpha \frac{\partial \rho}{\partial r_{1\alpha}}, \tag{56}$$

$$\frac{\partial u_\alpha}{\partial t_1} = -\frac{T}{\rho}\frac{\partial \rho}{\partial r_{1\alpha}} - \frac{\partial T}{\partial r_{1\alpha}} - u_\beta \frac{\partial u_\alpha}{\partial r_{1\beta}}, \tag{57}$$

$$\frac{\partial T}{\partial t_1} = -u_\alpha \frac{\partial T}{\partial r_{1\alpha}} - \frac{2}{D} T \frac{\partial u_\alpha}{\partial r_{1\alpha}}. \tag{58}$$

Then, the first-order approximation of the actual velocity distribution function f is

$$f \approx f^{eq} + \varepsilon f^{(1)} = f^{eq}\left(1 + D_\rho \left(\frac{\partial \rho}{\partial t} + v_\alpha \frac{\partial \rho}{\partial r_\alpha} \right) + D_T \left(\frac{\partial T}{\partial t} + v_\alpha \frac{\partial T}{\partial r_\alpha} \right) + D_{u_\beta} \left(\frac{\partial u_\beta}{\partial t} + v_\alpha \frac{\partial u_\beta}{\partial r_\alpha} \right) \right), \tag{59}$$

where $\frac{\partial}{\partial t} = \varepsilon \frac{\partial}{\partial t_1}$ and $\frac{\partial}{\partial r_\alpha} = \varepsilon \frac{\partial}{\partial r_{1\alpha}}$. For example, at the point $x = 0.38$ for Pr $= 1$ in Fig. 6, the ρ, u_α, T, and their corresponding time partial derivatives and space partial derivatives are calculated and shown in Table 1.

As a result, the actual distribution function at point $x = 0.38$ is obtained. The actual distribution function and its corresponding contour are shown in Fig. 8. The corresponding equilibrium distribution function is also plotted on the right hand — i.e., Figs. 8(b) and (d)—for

Table 1 The macroscopic quantities and their derivatives at point $x = 0.38$ for Pr $= 1$ in Fig. 6.

ρ	u_x	T	$\frac{\partial \rho}{\partial x}$	$\frac{\partial u_x}{\partial x}$	$\frac{\partial T}{\partial x}$	$\frac{\partial \rho}{\partial t}$	$\frac{\partial u_x}{\partial t}$	$\frac{\partial T}{\partial t}$
1.3190	0.5130	1.4858	−50.50	−61.55	−49.00	107.09	137.46	116.59

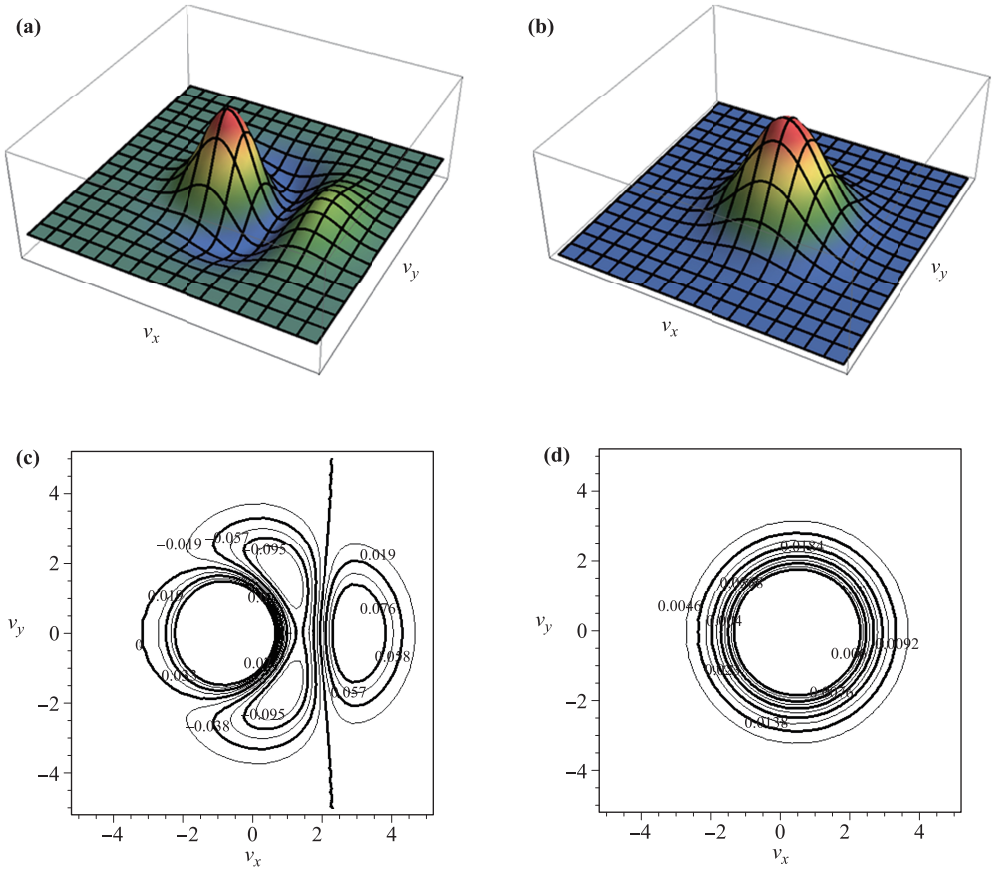

Fig. 8 The velocity distribution functions and their contour plot. **(a)** and **(c)** are first-order approximations of the actual distribution function and its contour plot. **(b)** and **(d)** are the corresponding local equilibrium distribution function and contour plot.

comparison. It can be found that the actual distribution function has two peaks in the x direction, which is a typical characteristic of shock waves [44].

Similarly, the second-order or higher-order approximation of the actual distribution function can also be recovered in the same way if it is necessary. It should be noted that the second-order space derivatives will be needed for second-order approximation of the actual distribution function, and the mth-order space derivatives will be needed for the mth approximation. Of course, the accuracy of the corresponding space derivatives needs to be guaranteed. The actual distribution of the discrete ES-BGK model can also be recovered by taking account the f^{ES} terms. In addition, this idea of recovering the actual distribution function by macroscopic quantities and their space derivatives is also applied for the NS equations and Burnett equations.

7 Conclusions

Under the framework of the CE multiscale analysis, a scheme for constructing a discrete ES-BGK model is presented. Compared with the original discrete BGK model, the new model works in a wider range of Knudsen numbers and has a flexible Prandtl number. As an example, the discrete ES-BGK model in the Burnett level is illustrated; the viscous stress and heat flux in the Burnett equations are related to the nonequilibrium quantities. The new model is verified by four numerical tests. When the system is near its thermodynamic equilibrium state, the NS viscous stress and heat flux work well. With the increasing of nonequilibrium strength, the NS viscous stress and heat flux should be replaced by the Burnett ones. When the nonequilibrium strength further increases, the viscous stress and heat flux should include higher-order nonequilibrium effects. Correspondingly, more kinetic moments of the equilibrium distribution function are generally needed in the model construction. In addition, a new scheme is proposed to recover quantitatively the main feature of the actual velocity distribution function from the macroscopic quantities and their space derivatives. Such a recovery method is needed when the distribution function is used to characterize the nonequilibrium state of the flow system. It works not only for simulations based on DBM, but also

for those based on hydrodynamic models, such as the NS and Burnett equations.

Acknowledgements The authors would like to acknowledge the support of the National Natural Science Foundation of China (Grant Nos. 11475028, 11772064, 11502117, and U1530261), and Science Challenge Project (Grant Nos. JCKY2016212A501 and TZ2016002).

References

1. H. Tsien, Superaerodynamics, Mechanics of Rarefied Gases, Collected Works of H. S. Tsien, 13(12), 406 (2012)
2. S. Ching, Rarefied Gas Dynamics, Berlin Heidelberg: Springer, 2005
3. W. Chen, W. Zhao, Z. Jiang, et al., A review of moment equations for rarefied gas dynamics, *Physics of Gases* 1(5), 9 (2016)
4. C. Ho and Y. Tai, Micro-electro-mechanical-systems (MEMS) and fluid flows, *Annu. Rev. Fluid Mech.* 30(1), 579 (1998)
5. G. Karniadakis and A. Beşkök, Microflows: Fundamentals and Simulation, Springer, 2005
6. Y. Zheng and H. Struchtrup, Burnett equations for the ellipsoidal statistical BGK model, *Contin. Mech. Thermodyn.* 16(1–2), 97 (2004)
7. L. Wu, C. White, T. J. Scanlon, J. M. Reese, and Y. Zhang, Deterministic numerical solutions of the Boltzmann equation using the fast spectral method, *J. Comput. Phys.* 250(250), 27 (2013)
8. G. A. Bird, Molecular Gas Dynamics and the Direct Simulation of Gas Flows, Oxford: Clarendon Press, 2003
9. K. Xu and J. C. Huang, A unified gas-kinetic scheme for continuum and rarefied flows, *J. Comput. Phys.* 229(20), 7747 (2010)
10. C. Liu, K. Xu, Q. Sun, et al., A unified gas-kinetic scheme for continuum and rarefied flows (IV), *Commun. Comput. Phys.* 14(5), 1147 (2014)
11. L. Yang, C. Shu, J. Wu, and Y. Wang, Numerical simulation of flows from free molecular regime to continuum regime by a DVM with streaming and collision processes, *J. Comput. Phys.* 306, 291 (2016)
12. Z. Guo, K. Xu, and R. Wang, Discrete unified gas kinetic scheme for all Knudsen number flows: Low-speed isothermal case, *Phys. Rev. E* 88(3), 033305 (2013)
13. Z. Guo, R. Wang, and K. Xu, Discrete unified gas kinetic scheme for all Knudsen number flows (II): Thermal compressible case, *Phys. Rev. E* 91(3), 033313 (2015)
14. Y. Zhang, R. Qin, and D. Emerson, Lattice Boltzmann simulation of rarefied gas flows in microchannels, *Phys. Rev. E* 71(4), 047702 (2005)
15. Y. Zhang, R. Qin, Y. Sun, R. W. Barber, and D. R. Emerson, Gas flow in microchannels–a lattice Boltzmann method approach, *J. Stat. Phys.* 121(1–2), 257 (2005)
16. X. Shan, X. F. Yuan, and H. Chen, Kinetic theory representation of hydrodynamics: a way beyond the Navier–Stokes equation, *J. Fluid Mech.* 550(-1), 413 (2006)
17. J. Meng, Y. Zhang, N. G. Hadjiconstantinou, G. A. Radtke, and X. Shan, Lattice ellipsoidal statistical BGK model for thermal non-equilibrium flows, *J. Fluid Mech.* 718, 347 (2013)
18. M. Watari, Is the lattice Boltzmann method applicable to rarefied gas flows? Comprehensive evaluation of the higher-order models, *J. Fluids Eng.* 138(1), 011202 (2015)
19. A. Xu, G. Zhang, and Y. Ying, Progress of discrete Boltzmann modeling and simulation of combustion system, *Acta Physica Sinica* 64(18), 184701 (2015)
20. A. Xu, G. Zhang, and Y. Gan, Progress in studies on discrete Boltzmann modeling of phase separation process, *Mech. Eng.* 38(4), 361 (2016)
21. A. Xu, G. Zhang, Y. Ying, et al., Complex fields in heterogeneous materials under shock: Modeling, simulation and analysis, *Sci. China: Phys. Mech. & Astron.* 59(5), 650501 (2016)
22. Y. Gan, A. Xu, G. Zhang, and S. Succi, Discrete Boltzmann modeling of multiphase flows: hydrodynamic and thermodynamic non-equilibrium effects, *Soft Matter* 11(26), 5336 (2015)
23. H. Lai, A. Xu, G. Zhang, Y. Gan, Y. Ying, and S. Succi, Nonequilibrium thermohydrodynamic effects on the Rayleigh-Taylor instability in compressible flows, *Phys. Rev. E* 94(2), 023106 (2016)
24. F. Chen, A. Xu, and G. Zhang, Viscosity, heat conductivity, and Prandtl number effects in the Rayleigh–Taylor Instability, *Front. Phys.* 11(6), 114703 (2016)
25. C. Lin, A. Xu, G. Zhang, and Y. Li, Double-distribution-function discrete Boltzmann model for combustion, *Combust. Flame* 164, 137 (2016)
26. Y. Zhang, A. Xu, G. Zhang, C. Zhu, and C. Lin, Kinetic modeling of detonation and effects of negative temperature coefficient, *Combust. Flame* 173, 483 (2016)
27. C. Lin, A. Xu, G. Zhang, Y. Li, and S. Succi, Polar-coordinate lattice Boltzmann modeling of compressible flows, *Phys. Rev. E* 89(1), 013307 (2014)
28. H. Liu, W. Kang, Q. Zhang, Y. Zhang, H. Duan, and X. T. He, Molecular dynamics simulations of microscopic structure of ultrastrong shock waves in dense helium, *Front. Phys.* 11(6), 115206 (2016)
29. H. Liu, Y. Zhang, W. Kang, P. Zhang, H. Duan, and X. T. He, Molecular dynamics simulation of strong shock waves propagating in dense deuterium, taking into consideration effects of excited electrons, *Phys. Rev. E* 95(2), 023201 (2017)

30. H. Liu, W. Kang, H. Duan, P. Zhang, and X. T. He, Recent progresses on numerical investigations of microscopic structure of strong shock waves in fluid, *Sci. China: Phys. Mech. & Astron.* 47(7), 070003 (2017)

31. W. Kang, U. Landman, and A. Glezer, Thermal bending of nanojets: Molecular dynamics simulations of an asymmetrically heated nozzle, *Appl. Phys. Lett.* 93(12), 123116 (2008)

32. P. L. Bhatnagar, E. P. Gross, and M. Krook, A model for collision processes in gases (I): Small amplitude processes in charged and neutral one-component systems, *Phys. Rev.* 94(3), 511 (1954)

33. Holway, New statistical models for kinetic theory: Methods of construction, *Phys. Fluids* 9(9), 1658 (1966)

34. E. M. Shakhov, Generalization of the Krook kinetic relaxation equation, *Fluid Dyn.* 3(5), 95 (1972)

35. V. A. Rykov, A model kinetic equation for a gas with rotational degrees of freedom, *Fluid Dyn.* 10(6), 959 (1976)

36. P. Andries, P. Le Tallec, J. P. Perlat, and B. Perthame, The Gaussian-BGK model of Boltzmann equation with small Prandtl number, *Eur. J. Mech. BFluids* 19(6), 813 (2000)

37. Y. Zheng and H. Struchtrup, Burnett equations for the ellipsoidal statistical BGK model, *Contin. Mech. Thermodyn.* 16(1–2), 97 (2004)

38. Y. Gan, A. Xu, G. Zhang, and Y. Yang, Lattice BGK kinetic model for high-speed compressible flows: Hydrodynamic and nonequilibrium behaviors, *EPL* 103(2), 24003 (2013)

39. H. Struchtrup, Macroscopic Transport Equations for Rarefied Gas Flows, Berlin Heidelberg: Springer, 2005

40. M. Watari and M. Tsutahara, Two-dimensional thermal model of the finite-difference lattice Boltzmann method with high spatial isotropy, *Phys. Rev. E* 67(3), 036306 (2003)

41. K. Xu, A gas-kinetic BGK Scheme for the Navier-Stokes equations and its connection with artificial dissipation and Godunov method, *J. Comput. Phys.* 171(1), 289 (2001)

42. Z. Guo, C. Zheng, and B. Shi, An extrapolation method for boundary conditions in lattice Boltzmann method, *Phys. Fluids* 14(6), 2007 (2002)

43. P. Woodward and P. Colella, The numerical simulation of two-dimensional fluid flow with strong shocks, *J. Comput. Phys.* 54(1), 115 (1984)

44. G. Pham-Van-Diep, D. Erwin, and E. P. Muntz, Nonequilibrium molecular motion in a hypersonic shock wave, *Science* 245(4918), 624 (1989)